Research Article Vol. 34, No. 8 / 20 Apr 2026 / Optics Express 14378
Optics EXPRESS

# Optical fiber–based nanoindenter featuring automated measurement

WEIDA HUANG,[1,2] YUXIN WANG,[1,2] FAMEI WANG,[3] MENGQIANG ZOU,[4] DEJUN LIU,[1,2] YING WANG,[1,2] YIPING WANG,[1,2] CHANGRUI LIAO,[1,2,6] AND GUISHENG WANG[5,7]

[1]*State Key Laboratory of Radio Frequency Heterogeneous Integration, Key Laboratory of Optoelectronic Devices and Systems of Ministry of Education/Guangdong Province, College of Physics and Optoelectronic Engineering, Shenzhen University, Shenzhen 518060, China*
[2]*Shenzhen Key Laboratory of Ultrafast Laser Micro/Nano Manufacturing, Guangdong and Hong Kong Joint Research Centre for Optical Fibre Sensors, Shenzhen University, Shenzhen 518060, China*
[3]*Shenzhen Key Laboratory of Ultra-Intense Laser and Advanced Material Technology, Center for Intense Laser Application Technology, and College of Engineering Physics, Shenzhen Technology University, Shenzhen 518118, China*
[4]*School of Electronic Science and Engineering, Chongqing University of Posts and Telecommunications, Chongqing 400065, China*
[5]*Department of Radiology, The Third Medical Centre, Chinese PLA General Hospital, Beijing 100039, China*
[6]*cliao@szu.edu.cn*
[7]*wangguisheng@301hospital.com.cn*

**Abstract:** Nanoindentation is a widely used technique for localized mechanical characterization at the micro- and nanoscale, where measurement accuracy critically depends on high-resolution sensing and signal readout mechanisms. In this work, we present an improved fiber-optic nanomechanical probe (FONP) fabricated by femtosecond laser two-photon polymerization and develop a dedicated fiber-optic nanoindentation system specifically designed for automated measurements. The enhanced FONP employs Fabry–Pérot interferometric optical readout and incorporates an optical shielding layer that ensures spectral stability during surface approach without requiring a gold coating, maintaining a cross-correlation coefficient of 1 with the reference spectrum. Using the developed system, we investigate the time-dependent mechanical evolution of onion outer epidermal cells during natural dehydration, revealing a clear increase in Young's modulus. In addition, automated array-based Young's modulus mapping of polydimethylsiloxane (PDMS) samples shows strong agreement with a commercial nanoindenter, with deviations within 10%. These results demonstrate the accuracy, stability, and automation capability of the proposed fiber-optic interferometric nanoindentation system, highlighting its potential for compact and robust nanomechanical characterization.



## 1. Introduction

Nanoindentation is a widely adopted technique for localized mechanical characterization at the micro- and nanoscale [1–3], in which measurement accuracy and reliability critically depend on the underlying sensing and signal readout mechanisms. Although traditionally viewed as a mechanical testing method [4–6], modern nanoindentation increasingly relies on advanced optical techniques to achieve high-resolution force and displacement measurements. In particular, fiber-optic and interferometric sensing approaches offer distinct advantages, including high sensitivity, immunity to electromagnetic interference, and strong potential for system miniaturization and automation [7–9].

#596766 https://doi.org/10.1364/OE.596766
Journal © 2026 Received 2 Mar 2026; revised 19 Mar 2026; accepted 23 Mar 2026; published 8 Apr 2026

Optics EXPRESS

Nanoindentation determines mechanical properties by applying small forces to a material surface and recording the corresponding load–displacement response, from which parameters such as hardness and elastic modulus can be extracted [10,11]. Conventional commercial nanoindenters predominantly employ electrical or MEMS-based force and displacement sensing architectures. Although these systems offer high resolution, their electrical demodulation circuits are inherently sensitive to thermal drift and electromagnetic interference, which can significantly degrade signal stability and measurement accuracy. Moreover, the complexity of these sensing architectures results in bulky instrument configurations and limited portability.

Optical approaches provide an attractive alternative for nanoscale mechanical sensing owing to their high sensitivity, immunity to electromagnetic interference, and potential for miniaturization. Atomic force microscopy (AFM), which relies on the optical lever principle, represents a typical optical readout strategy for nanoscale force measurement [12–14]. However, AFM requires a precisely aligned free-space optical path, leading to complex calibration procedures and reduced robustness, particularly in long-term or automated measurements.

To overcome these limitations, we previously proposed a miniaturized fiber-optic nanomechanical probe fabricated by femtosecond laser two-photon polymerization [15]. The FONP integrates a mechanically compliant microstructure directly onto the end face of an optical fiber and employs Fabry–Pérot interferometric sensing for force and displacement readout. This all-fiber optical configuration enables high-resolution mechanical sensing while eliminating free-space optical alignment. In addition, the probe stiffness can be flexibly engineered through geometric design, allowing adaptation to materials with a wide range of mechanical properties [16].

Building upon this optical sensing architecture, the present work reports the development of a fully automated fiber-optic nanoindentation system centered on the FONP. By integrating interferometric optical readout with a custom positioning platform and self-developed control software, the system enables automated indentation and spatially resolved mechanical mapping. The proposed approach demonstrates how fiber-optic interferometric sensing can be leveraged to realize compact, stable, and automation-ready nanoindentation instrumentation, highlighting its potential for advanced nanomechanical characterization in both material and biological applications.

## 2. Working principle

The micro-cantilever probe was fabricated on the end face of an optical fiber using femtosecond laser two-photon polymerization (TPL) through a three-step process consisting of photoresist dispensing, laser polymerization, and development [17–20]. This fabrication approach produces a cantilever-beam structure with characteristic dimensions on the order of hundreds of micrometers [21]. Together with the fiber end face, the cantilever forms an optical Fabry–Pérot (FP) microcavity, as illustrated in Fig. 1(a), which serves as the core sensing element of the fiber-optic nanomechanical probe. Micro-scale forces applied to the probe are detected by demodulating the reflection spectrum of this FP microcavity.

The FP microcavity is a widely employed interferometric structure in optical sensing. It consists of two parallel reflective surfaces, between which incident light undergoes multiple reflections, producing an interference pattern in the reflected spectrum [22–24]. In the FONP, the air gap between the micro-cantilever and the fiber end face defines the FP cavity, with these two interfaces acting as the interferometric mirrors.

When an external force is applied to the probe tip, the micro-cantilever deflects, leading to a change in the cavity length D. The resonant wavelength λ of the FP interference spectrum is directly related to the cavity length according to [23]

$$\lambda = \frac{2nD}{m} \tag{1}$$

Optics EXPRESS

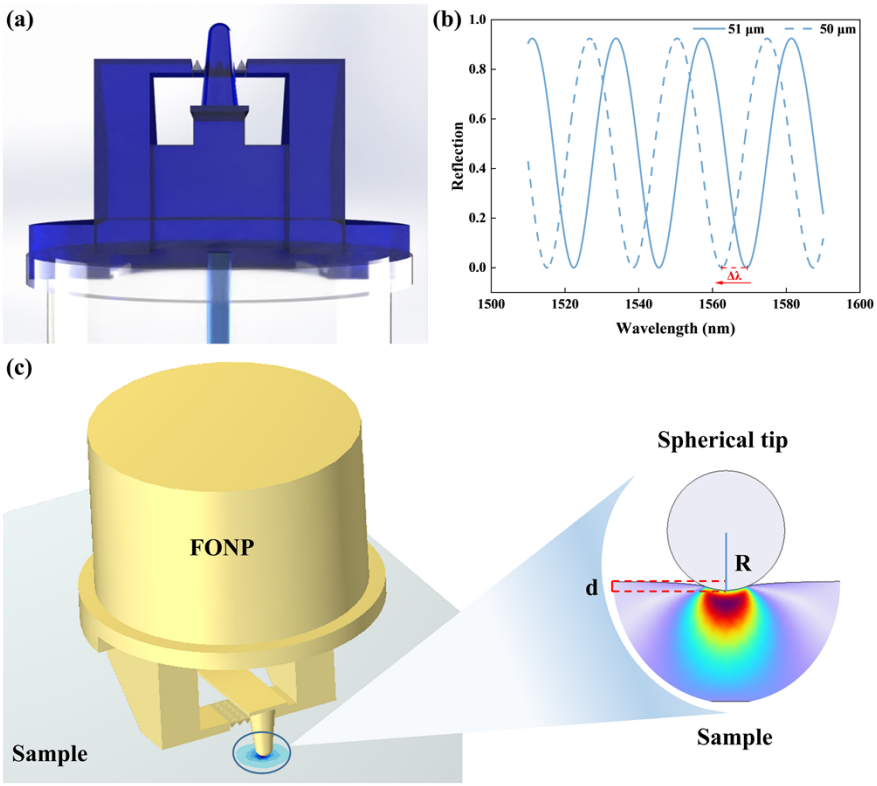


**Fig. 1.** Optical interferometric working principle of the fiber-optic nanomechanical probe (FONP). (a) Schematic structure of the FONP, in which a micro-cantilever fabricated on the fiber end face forms a Fabry–Pérot (FP) microcavity. (b) Dip wavelength shift of the FP interference spectrum induced by force-driven cantilever deflection. (c) FONP-based nanoindentation measurement.

Where m is the interference order, n is the refractive index of the medium within the cavity. As a result, force-induced cantilever deflection produces a measurable shift in the resonant wavelength, as schematically shown in Fig. 1(b). By tracking this wavelength shift and correlating it with the mechanical response of the cantilever, the applied force can be quantitatively determined.

To convert the optical wavelength shift into mechanical information, prior calibration of the cantilever is required. The elastic constant $K$ of the micro-cantilever defines the relationship between the applied force F and the resulting deflection d:

$$F = K \cdot \mathrm{d} \tag{2}$$

For a rectangular cantilever beam, the elastic constant is governed by its geometric parameters and material properties and can be expressed as [15]

$$K = \frac{Ebt^3}{4L^3} \tag{3}$$

where $E$ is the Young's modulus of the cantilever material, and $b$, $t$, and $L$ denote the width, thickness, and length of the cantilever, respectively. The elastic constant of the probe is experimentally calibrated using a reference material. Subsequently, the calibrated probe is indented into a rigid glass substrate. Owing to the large stiffness mismatch between the polymer

Optics EXPRESS

cantilever and the glass, the cantilever deflection at each displacement step closely approximates the imposed displacement. Under this condition, the observed resonant wavelength shift can be directly mapped to the applied force, enabling accurate force calibration of the FP optical readout.

During nanoindentation, the FONP allows the simultaneous acquisition of force–displacement data. Combined with the known probe geometry, this information enables the extraction of the sample's Young's modulus.

For data analysis, classical nanoindentation methods such as the Oliver–Pharr model are commonly employed. This method determines elastic modulus and hardness by fitting the unloading curve to obtain the contact stiffness and projected contact area. However, its accuracy strongly depends on precise calibration of the probe area function and may be compromised when applied to fully plastic or viscoelastic materials [25].

In this work, the Hertzian contact model is adopted to analyze indentation data. Originally developed to describe elastic contact between two solids, the Hertz model is particularly well suited for soft materials and thin films. For a spherical indenter, the force–displacement relationship is given by [26]

$$F = \frac{4}{3}\frac{E}{(1-\nu^2)}\sqrt{R}d^{\frac{3}{2}} \tag{4}$$

where $F$ represents the external force, and d represents the indentation distance, and $E$ and ν are the Young's modulus and Poisson's ratio of the sample, respectively, and R is the radius of the spherical indenter. Unlike the Oliver–Pharr approach, which relies on unloading data, the Hertzian model utilizes the loading curve and assumes purely elastic deformation. This feature enables high-precision mechanical characterization of soft and viscoelastic materials under small deformations, making it particularly suitable for fiber-optic nanoindentation applications.

## 3. System composition

The fiber-optic nanoindentation instrument developed in this work is a highly integrated and automated measurement system. It consists of a fiber-optic nanomechanical probe (FONP), a probe positioning stage, a sample positioning stage, an inverted optical microscope, and a spectral demodulation unit. These components are coordinated to enable real-time optical sensing, automated probe–sample interaction and spatially resolved mechanical characterization.

### *3.1. Optical characterization and shielding performance*

Accurate determination of the probe state is essential for automated nanoindentation. In the proposed system, the real-time Fabry–Pérot (FP) interference spectrum of the FONP serves as a direct optical indicator of probe–sample interaction. By continuously acquiring the reflection spectrum and tracking characteristic spectral features, the probe state—including free approach and initial contact—can be reliably identified without additional force or displacement sensors.

Following fabrication by two-photon polymerization, conventional approaches coat the cantilever surface with a thin gold layer to suppress stray light and stabilize the FP cavity. However, selective gold deposition exclusively on the cantilever, without contaminating the fiber core end-face, is technically challenging and highly sensitive to sputtering alignment. Moreover, metal coatings may introduce additional optical loss and long-term stability issues.

To overcome these limitations, we designed a monolithic optical shielding layer integrated directly into the cantilever structure, eliminating the need for metallic coatings. This shielding structure exploits total internal reflection (TIR) to optically isolate the FP cavity from the surrounding environment and the sample surface, thereby suppressing parasitic reflections and preventing the formation of spurious FP cavities during surface approach.

Given a refractive index of 1.53 for the polymerized photoresist, the critical angle for TIR at the polymer–air interface is approximately 40.81°. A pyramid array was designed on the upper surface of the cantilever, with each pyramid having a square base of 4 μm × 4 μm and a height

Optics EXPRESS

4 µm. When sensing light propagating from the fiber end-face reaches the polymer–air interface at an incident angle of 54.73°, the TIR condition is satisfied, effectively confining the optical field within the probe structure and preventing stray light leakage.

An FONP incorporating the optical shielding layer was successfully fabricated on the fiber end-face. Scanning electron microscopy (SEM) images in Figs. 2(a) and 2(b) reveal the cantilever, probe tip, reinforcement structure, and the integrated shielding layer. The fabricated pyramid array exhibits a measured height of 5.8 µm and a base side length of 4.6 µm, corresponding to an incident angle of approximately 64.59°, well above the critical angle, thereby ensuring complete total internal reflection. The different between the fabricated results and the designed model parameters is primarily attributed to the Z-axis stretching of the femtosecond laser focal spot. However, this specific fabrication outcome increases the incident angle at the inner interface, thereby benefiting the total internal reflection condition. The reflection spectrum of the shielded FONP, shown in Fig. 2(c), exhibits a free spectral range (FSR) of 25.31 nm. The relationship between the FSR and the FP cavity length D is given by

$$FSR = \frac{\lambda^2}{2n\mathrm{D}} \tag{5}$$

where $\lambda$ is the resonant wavelength and n is the refractive index of the cavity medium. Using Eq. (5), the cavity length is calculated to be 47.6 µm, in close agreement with the value of 47.9 µm measured by optical microscopy.

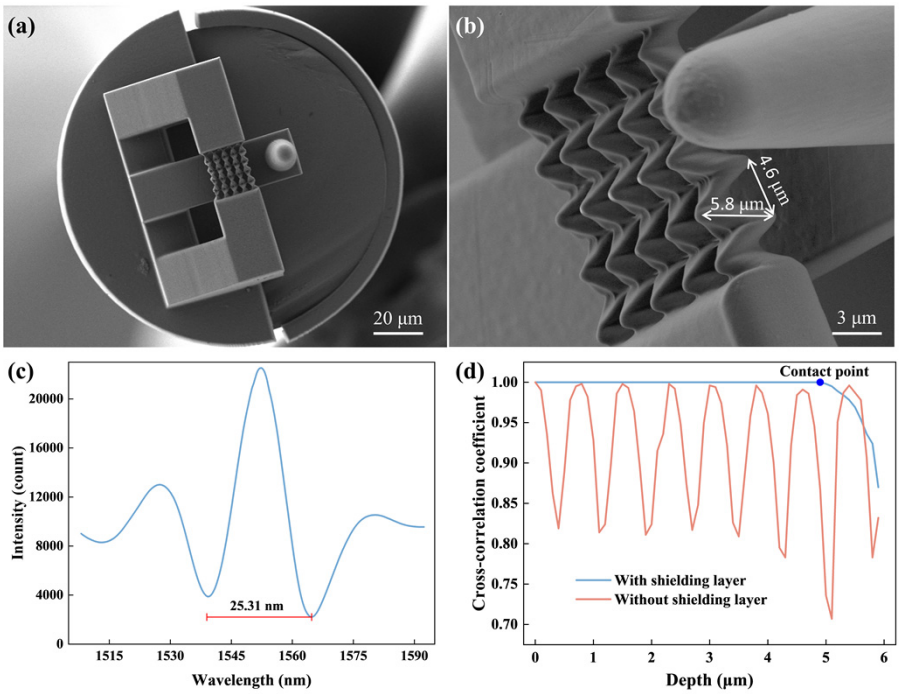


**Fig. 2.** FONP with an integrated optical shielding layer: (a) SEM image of the probe, (b) schematic of the shielding structure, (c) FP reflection spectrum, and (d) comparison of cross-correlation coefficients during surface approach with and without shielding

To quantitatively evaluate spectral stability during probe approach, a cross-correlation-based demodulation strategy was employed. At the beginning of the approach, the initial FP spectrum is stored as a reference. During subsequent approach steps, the cross-correlation coefficient

Optics EXPRESS

between the live spectrum and the reference is computed in real time. A coefficient approaching unity indicates high spectral similarity, while a sudden decrease signifies a significant spectral shift associated with probe–sample contact [27,28].

Stepwise approach experiments were performed using FONPs with and without the optical shielding layer, and the corresponding cross-correlation responses are shown in Fig. 2(d). For the shielded probe, the coefficient remains at unity prior to contact, indicating excellent spectral stability, and decreases monotonically upon contact. In contrast, the unshielded probe exhibits continuous fluctuations throughout the approach, with no clear transition point. These results demonstrate that the optical shielding layer enables reliable, threshold-based contact detection and forms the foundation for automated nanoindentation.

### 3.2. System integration and automated measurement workflow

Precise spatial localization of indentation points is achieved using an inverted optical microscope system comprising a white light source, mirrors, a dichroic mirror, an objective lens, and a CCD camera. The probe positioning unit integrates a three-axis manual translation stage, a single-axis piezoelectric actuator, and a fiber clamp to ensure alignment and perpendicularity between the probe and the sample surface.

For fine positioning, a linear nanopositioning stage (PI, P-631.XCD) with an 80 µm travel range and 0.1 nm resolution was employed. The sample stage combines a two-axis coarse positioning stage with a three-axis nanopositioning stage (PI, P-561.3CD), providing a 100 µm travel range and 0.8 nm resolution on each axis. Optical spectral demodulation is performed using an FBG interrogator (Bayspec, WaveCapture) operating from 1510 to 1590 nm with a wavelength resolution of 175 pm.

All hardware components are synchronized through a centralized control program developed in LabVIEW, enabling automated probe approach, indentation, spectral acquisition, and mechanical data extraction. The fully integrated system configuration is shown in Fig. 3(a).

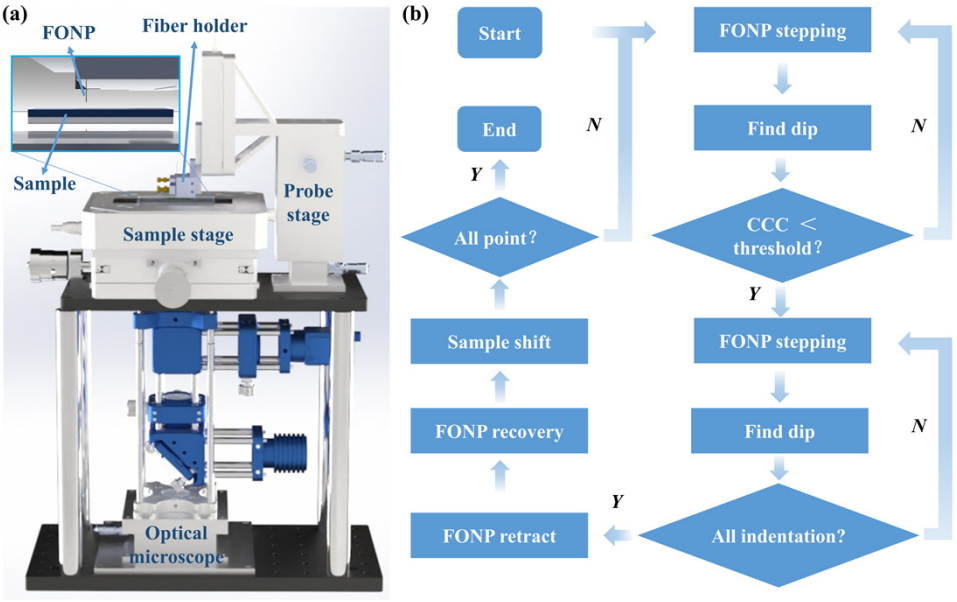


**Fig. 3.** Fiber-optic nanoindentation instrument: (a) system configuration and (b) flowchart of the automated nanoindentation procedure.

Optics EXPRESS

The automated measurement workflow, illustrated in Fig. 3(b), consists of three stages: surface approach, single-point indentation, and sample repositioning. During surface approach, the probe advances toward the sample in discrete steps, and the cross-correlation coefficient is evaluated after each step. Once the coefficient drops below a predefined threshold, contact is detected and indentation is initiated. After completing a single indentation, the probe retracts to a safe height, the sample is repositioned, and the process repeats to enable array-based measurements. It is worth noting that to eliminate potential interference from environmental fluctuations during prolonged measurements, reference spectrum calibration is performed immediately prior to each individual indentation.

For soft materials, the probe step distance dp is composed of the cantilever deflection dc and the sample indentation depth $d_i$:

$$d_p = d_c + d_i \tag{6}$$

Using the calibrated force–wavelength relationship, the applied force $F$ corresponding to dc is determined, and the indentation depth is calculated as

$$d_i = d_p - d_c = d_p - \frac{F}{K} \tag{7}$$

The resulting force–indentation data are then fitted using an appropriate contact mechanics model corresponding to the probe tip geometry to extract the Young's modulus of the sample.

## 4. Sample measurement

In this section, single-point and array-based Young's modulus measurements were performed using the fabricated FONP and the fiber-optic nanoindentation instrument. All results were obtained after mechanical calibration of the probe and were systematically compared with those from a commercial nanoindenter to validate accuracy and reliability.

### 4.1. Mechanical calibration of the FONP

Prior to sample measurements, mechanical calibration of the FONP was conducted. The probe was positioned several micrometers above a rigid glass substrate, and the automated surface-detection routine was executed within the 80 μm travel range of the piezoelectric stage. Upon surface detection, the probe indented the glass substrate using predefined step parameters. The resulting relationship between cantilever deflection and resonant wavelength is shown in Fig. 4(a).

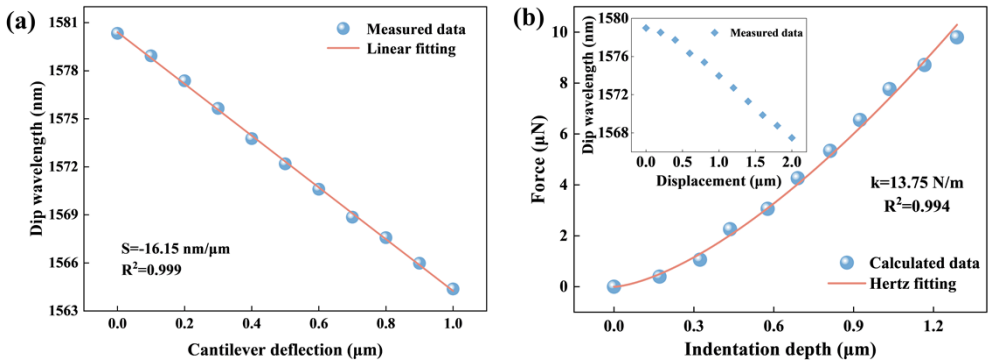


**Fig. 4.** Mechanical calibration of the FONP: (a) cantilever deflection versus dip wavelength and (b) elastic constant calibration using a reference PDMS sample.

To establish the quantitative relationship between resonant wavelength and applied force, the elastic constant K of the cantilever was calibrated using a reference-material-based method,

Optics EXPRESS

analogous to that employed in commercial nanoindentation systems. A PDMS sample with a known Young's modulus was used as the reference material. Nanoindentation experiments were performed on the PDMS sample (Fig. 4(b)), and the step distance–resonant wavelength data were converted into force–indentation curves using different trial values of K. These curves were fitted with the Hertzian contact model, and the value of K that yielded the best agreement with the known PDMS modulus was selected. With both the deflection–wavelength relationship and the calibrated elastic constant determined, the resonant wavelength–force mapping of the FONP was uniquely established.

### 4.2. Single-point measurements on onion epidermal cells

Following calibration, single-point nanoindentation measurements were conducted on onion outer epidermal cells. The cells were allowed to undergo natural dehydration under ambient conditions, and measurements were performed at regular time intervals to investigate time-dependent mechanical evolution, as summarized in Fig. 5.

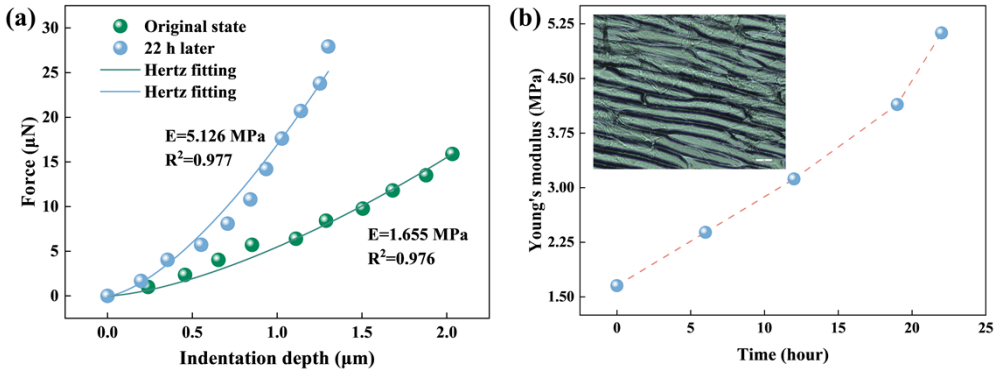


**Fig. 5.** Mechanical characterization of onion epidermal cells: (a) representative nanoindentation curves at 0 h and 22 h and (b) temporal evolution of Young's modulus.

The epidermal cells were peeled from an onion, flattened on a glass slide, and placed on the sample stage. Nanoindentation was performed using a step size of 0.3 μm and 10 indentation steps. Using the calibrated force–wavelength relationship, the measured wavelength–displacement data were converted into force–indentation curves and fitted using the Hertzian contact model. The maximum indentation depth was approximately 2 μm, which is safely below 10% of the typical thickness of an onion epidermal cell (20–30 μm) [29]. Therefore, measurement errors induced by the substrate effect can be essentially neglected. The initial Young's modulus was determined to be 1.655 MPa. As dehydration progressed, the Young's modulus increased monotonically, reaching 5.126 MPa after 22 h. This trend indicates an inverse relationship between water content and mechanical stiffness, consistent with previously reported observations for plant cells [30]. These results demonstrate the capability of the proposed system to resolve subtle mechanical variations in soft biological samples.

### 4.3. Automated array measurements on PDMS

To further validate system accuracy, stability, and automation capability, array-based Young's modulus mapping was performed on PDMS samples. The PDMS surface was observed using the inverted optical microscope, and a suitable measurement region was selected. Automated array measurements were then carried out using the programmed routine without manual intervention. The resulting $10 \times 10$ Young's modulus map is shown in Fig. 6(a).

Optics EXPRESS

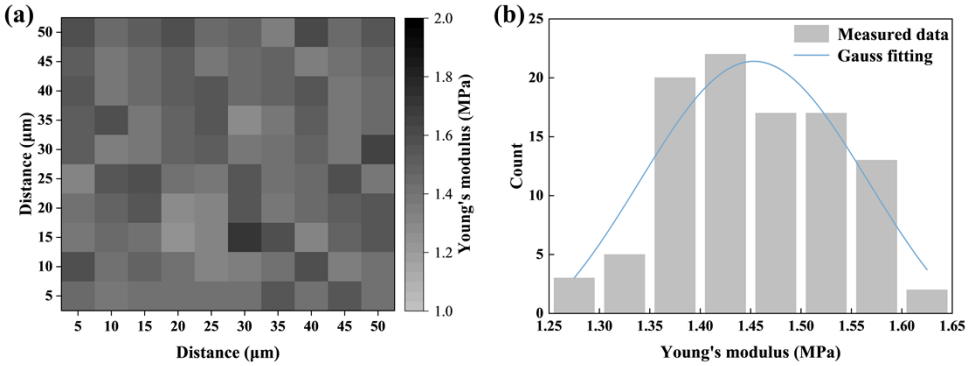


**Fig. 6.** Young's modulus mapping of PDMS: (a) $10 \times 10$ array measurement results and (b) frequency distribution of Young's modulus values

All 100 measurement points exhibited coefficients of determination ($R^2$) exceeding 0.98. The complete array measurement was completed within 15 minutes, corresponding to an average acquisition time of approximately 9 s per point, and proceeded without interruption. The measured Young's modulus values ranged from 1.252 MPa to 1.708 MPa, with a mean value of 1.457 MPa. This value shows excellent agreement with the reference modulus of 1.454 MPa obtained using a commercial nanoindenter, corresponding to a deviation of less than 10%. The frequency distribution of the measured moduli follows a Gaussian profile (Fig. 6(b)). A Gaussian fit yields a central value of 1.453 MPa, further confirming the high accuracy, repeatability, and robustness of the fiber-optic nanoindentation system.

## 5. Conclusion

In this work, a fiber-optic nanomechanical probe was fabricated on the end face of an optical fiber using femtosecond laser two-photon polymerization. A monolithic optical shielding layer was integrated into the probe, effectively suppressing parasitic optical cavities and significantly enhancing spectral stability during surface approach. Based on the FONP, a compact fiber-optic nanoindentation instrument was developed, in which Fabry–Pérot interferometric sensing serves as the core optical readout. Fully automated acquisition and analysis of Young's modulus were realized through a dedicated LabVIEW-based control program.

Using the developed system, time-resolved nanoindentation measurements on onion outer epidermal cells revealed a progressive increase in Young's modulus during natural dehydration, demonstrating sensitivity to subtle mechanical variations in soft biological samples. Automated $10 \times 10$ array measurements on PDMS samples showed excellent agreement with a commercial nanoindenter, with deviations within 10%. All indentation curves exhibited coefficients of determination ($R^2$) exceeding 0.98, confirming high accuracy, repeatability, and operational stability. In addition, the system achieved a high throughput, with an average acquisition time of approximately 9 s per measurement point.

Limited by the intrinsic Young's modulus of the photopolymer material, the maximum measurable Young's modulus of the current system is capped at approximately 200 MPa. To broaden the measurable range in future applications, ceramic-doped photoresists could be developed and utilized to further enhance the intrinsic stiffness of the 3D-printed probe. Looking forward, the FONP holds significant potential for advanced biomedical applications, such as the continuous in situ monitoring of localized cellular stiffness changes during metastasis. Furthermore, by integrating a high-frequency driving module and dynamic spectral demodulation, the system could be upgraded to a dynamic non-contact operating mode.

Optics EXPRESS

The proposed FONP-based fiber-optic nanoindentation platform provides a versatile and extensible solution for optical interferometric mechanical sensing. Its all-fiber architecture, miniaturized probe, and robust spectral demodulation strategy make it well suited for applications in biomedical mechanics and soft material characterization. With minimal system modification, the platform can be readily extended to investigate time-dependent mechanical behaviors, including creep and viscoelasticity, highlighting its potential for dynamic nanomechanical studies.

**Funding.** National Key Research and Development Program of China (2024YFB3213700); National Natural Science Foundation of China (T2421003, 62475161, 62405040, 62305223); Key Area Project of the Department of Education of Guangdong Province (2025ZDZX3023); Research Team Cultivation Program of Shenzhen University (2023QNT009); Medicine Plus Program of Shenzhen University (2024YG013).

**Disclosures.** The authors declare no conflicts of interest.

**Data availability.** Data underlying the results presented in this paper are not publicly available at this time but may be obtained from the authors upon reasonable request.

## References

1. D. Zhu, S. Jiang, C. Liao, *et al.*, "Ultrafast Laser 3D Nanolithography of Fiber-Integrated Silica Microdevices," Nano Lett. **24**(31), 9734–9742 (2024).
2. G. Cao and H. Gao, "Mechanical properties characterization of two-dimensional materials via nanoindentation experiments," Prog. Mater. Sci. **103**, 558–595 (2019).
3. J. Guo, Z. Zhang, B. Yang, *et al.*, "Oxygen vacancy-induced strengthening and toughening in (K,Na)NbO3-based piezoceramics revealed via nanoindentation," Nat. Commun. **16**(1), 7015 (2025).
4. A. Nafari, A. Danilov, H. Rödjegård, *et al.*, "A micromachined nanoindentation force sensor," Sens. Actuators, A **123-124**, 44–49 (2005).
5. D. Lu, J. Liu, M. Wang, *et al.*, "State-of-the-Art Design and Optimization of Strain Gauge-Type Load–Displacement Transducer for in In Situ Nanoindentation Systems," Sensors **25**(3), 609 (2025).
6. D. A. Lucca, K. Herrmann, and M. J. Klopfstein, "Nanoindentation: Measuring methods and applications," CIRP Ann. **59**(2), 803–819 (2010).
7. L. Chen, B. Liu, C. Markwell, *et al.*, "A nanonewton force sensor using a U-shape tapered microfiber interferometer," Sci. Adv. **10**(22), eadk8357 (2024).
8. X. Shang, N. Wang, S. Cao, *et al.*, "Fiber-Integrated Force Sensor using 3D Printed Spring-Composed Fabry-Perot Cavities with a High Precision Down to Tens of Piconewton," Adv. Mater. **36**(2), 2305121 (2024).
9. Y. Liu, R. Zheng, S. Peng, *et al.*, "Highly Sensitive Fiber-Optic Fabry–Perot Microforce Probe," J. Lightwave Technol. **43**(1), 383–389 (2025).
10. N. K. Mukhopadhyay and P. Paufler, "Micro- and nanoindentation techniques for mechanical characterisation of materials," Int. Mater. Rev. **51**(4), 209–245 (2006).
11. P. Zhu, Y. Zhao, S. Agarwal, *et al.*, "Toward accurate evaluation of bulk hardness from nanoindentation testing at low indent depths," Mater. Des. **213**, 110317 (2022).
12. E. Siamantouras, C. Woodrow, E. Celiker, *et al.*, "Quantification of bush-cricket acoustic trachea mechanics using Atomic Force Microscopy nanoindentation," Acta Biomater. **153**, 399–410 (2022).
13. X. Deng, F. Xiong, X. Li, *et al.*, "Application of atomic force microscopy in cancer research," J. Nanobiotechnol. **16**(1), 102 (2018).
14. A. Lostao, K. Lim, M. C. Pallarés, *et al.*, "Recent advances in sensing the inter-biomolecular interactions at the nanoscale – A comprehensive review of AFM-based force spectroscopy," Int. J. Biol. Macromol. **238**, 124089 (2023).
15. M. Zou, C. Liao, Y. Chen, *et al.*, "3D printed fiber-optic nanomechanical bioprobe," Int. J. Extrem. Manuf. **5**(1), 015005 (2023).
16. F. Wang, M. Zou, C. Liao, *et al.*, "Three-dimensional printed microcantilever with mechanical metamaterial for fiber-optic microforce sensing," APL Photonics **8**(9), 096108 (2023).
17. M. Chen, S. Dong, S.-Y. Liu, *et al.*, "3D Printed Micro-Nano Waveguide Ultrashort Bragg Grating on Optical Fiber Tip as a Contact Liquid Reagent Temperature Sensor," J. Lightwave Technol. **42**(8), 3059–3064 (2024).
18. B. Nan, W. Bao, Z. Shao, *et al.*, "A 3D-Printed Multicore Fiber-Tip Resonator for Ultrasonic Sensing," ACS Photonics **12**(11), 6114–6121 (2025).
19. N. Hu, Y. Deng, L. Ding, *et al.*, "Micro-spring force sensors using conductive photosensitive resin fabricated via two-photon polymerization," Microsyst. Nanoeng. **11**(1), 149 (2025).
20. D. Zhu, S. Jiang, Y. Wang, *et al.*, "Three-dimensional direct lithography of stable quantum dots in hybrid glass," Int. J. Extrem. Manuf. **7**(3), 035503 (2025).
21. M.-Q. Chen, Z. Zhou, H. Li, *et al.*, "Research on Temperature and Strain Sensing of Novel Femtosecond Laser-Based Three-Core Optical Fiber Parallel Bragg Grating," IEEE Trans. Instrum. Meas **74**, 7000807 (2025).
22. M. Chen, Y. Zhao, H. Wei, *et al.*, "3D printed castle style Fabry-Perot microcavity on optical fiber tip as a highly sensitive humidity sensor," Sens. Actuators, B **328**, 128981 (2021).

Optics EXPRESS


23. M. Zou, C. Liao, S. Liu, *et al.*, "Fiber-tip polymer clamped-beam probe for high-sensitivity nanoforce measurements," Light:Sci. Appl. **10**(1), 171 (2021).
24. L. Zhang, X. Shang, S. Cao, *et al.*, "Optical steelyard: high-resolution and wide-range refractive index sensing by synergizing Fabry–Perot interferometer with metafibers," PhotoniX **5**(1), 24 (2024).
25. S. V. Kontomaris and A. Malamou, "Hertz model or Oliver & Pharr analysis? Tutorial regarding AFM nanoindentation experiments on biological samples," Mater. Res. Express **7**(3), 033001 (2020).
26. Z. Guo, M. Hao, L. Jiang, *et al.*, "A modified Hertz model for finite spherical indentation inspired by numerical simulations," European Journal of Mechanics - A/Solids **83**, 104042 (2020).
27. J. Zhang, X. Zhang, Z. Guo, *et al.*, "Fundamental and high-order cross-correlation combined demodulation method for absolute cavity length measurement of fiber-optic Fabry–Perot sensors," Opt. Eng. **61**(09), 096102 (2022).
28. H. Chen, J. Liu, X. Zhang, *et al.*, "High-Order Harmonic-Frequency Cross-Correlation Algorithm for Absolute Cavity Length Interrogation of White-Light Fiber-Optic Fabry-Perot Sensors," J. Lightwave Technol. **38**(4), 953–960 (2020).
29. C.-C. Chen, W.-P. Shih, P.-Z. Chang, *et al.*, "Onion artificial muscles," Appl. Phys. Lett. **106**(18), 183702 (2015).
30. D. J. Cosgrove, "Plant cell wall extensibility: connecting plant cell growth with cell wall structure, mechanics, and the action of wall-modifying enzymes," EXBOTJ **67**(2), 463–476 (2016).